Toward Prediction of Microstructural Evolution during Laser Surface Alloying

S.S. BABU, R.P. MARTUKANITZ, K.D. PARKS, and S.A. DAVID

The stability of tungsten carbide particles in iron-rich and nickel-rich liquid during the laser surface alloying (LSA) process was investigated. Kinetic calculations indicate a rapid dissolution of tungsten carbide particles in iron-rich liquid, as compared with the dissolution rate in nickel-rich liquid. Optical microscopy indicated a heterogeneous microstructure around the tungsten particles that is in agreement with concentration gradients predicted by kinetic calculations. The work demonstrates the applicability of computational thermodynamics and kinetic models for the LSA process.

I. INTRODUCTION

LASER surface alloying (LSA) is a versatile process, through which one can modify the surface properties of metals and ceramics to obtain required properties. The properties of the surface are modified by localized melting and solidification. The LSA process alters the solidified microstructure by alloy-induced transformations, composite strengthening through production of second-phase particles, or a combination of both.[1–5] A review of the literature shows that a variety of applications have been developed for LSA processes. The most common uses are for improving resistance to corrosion, abrasion, erosion, oxidation, and wear.[6–13] Applications include modification of surface properties for medical applications.[14] In other cases, rapid cooling rates were used to produce metallic glasses.[15] The properties of the LSA region depend on the microstructure which evolves during melting and cooling. One of the most common microstructural changes is the dissolution of primary phases in powders, leading to precipitation of complex phases during melting and subsequent solidification. For example, during LSA of nickel-based alloys with silicon carbide particles, the particles melt in the liquid pool, and, during subsequent solidification, M_7C_3 carbides* precipitate from the liquid.[16] Previous work has attempted to control the LSA microstructure by modifying the laser beam parameters and by changing the alloying additions through extensive experimental research.[17,18] Adding alloying elements to the molten pool modifies the liquid pool composition. The alloying elements are added either by preplacing powders on the substrate or by injecting them into the trailing edge of the molten pool. Some processes combine both methodologies. The major alloying elements are preplaced on the sample, and secondary alloying elements or particles are added to the trailing edge of the molten pool. It is important to note that the microstructural evolution in the alloyed regions is controlled by the thermal cycles experienced in these regions and by the stability of the various phases. The present work pertains to the development of models to predict the microstructural evolution during the LSA process. An ideal model would couple computational heat-transfer and fluid-flow models with computational thermodynamic and kinetic models to predict the microstructural evolution in the LSA regions.

Models for predicting microstructural evolution within the weld-metal zone have been developed during prior research.[19–22] Stability calculations made as part of the LSA design process describe each of the various phases as a function of temperature and alloying-element concentration.[6] However, no studies have addressed the effects of solidification, kinetics, or the applicability of computational thermodynamics when determining the stability of hard particles added during LSA. In this work, the stability of tungsten carbide (MC)* particles in iron-rich and nickel-rich alloy systems was evaluated with computational thermodynamic and kinetic calculations. This research will eventually form a basis for a robust predictive model that can predict the microstructural evolution in multicomponent, multiphase alloys during LSA processing.

*Here, the letter "M" corresponds to the metal content, including Fe, Cr, and other alloying additions.

*Here MC, a generic name of tungsten carbide, is used to be consistent with thermodynamic calculations.

II. EXPERIMENTAL

A Hobart Model HLP 3000 Nd:YAG laser system equipped with fiber optics was used for the LSA experiments. This system provides 3.0 kW output power at the source. A continuous-wave beam was delivered to the workpiece *via* a 600-μm-diameter fiber-optic cable that was attached to f16 optics; a transmissive lens produced a 4.8-mm-diameter defocused spot. The beam-energy distribution exiting the focusing optics was modified to a "top hat" configuration. The beam was manipulated by a linear-motion device. The power delivered from the system to the workpiece, measured by a water calorimeter, was 2.3 kW. Samples were shielded by argon flow at a rate of 11.8 L/min. The laser scanning speed varied over a range of 2.12 to 6.35 mm s^{-1} (Table I).

The LSA experiments were conducted by the addition of

S.S. BABU, R&D Staff Member, and S.A. DAVID, Group Leader and Corporate Fellow, are with the M&C Division, Oak Ridge National Laboratory, Oak Ridge, TN 37831-6095. Contact e-mail: babuss@ornl.gov. R.P. MARTUKANITZ, Assistant Director, is with the Laser Processing Division, Applied Research Laboratory, Pennsylvania State University, University Park, PA 16802. K.D. PARKS, formerly Research Staff Member, with the Laser Processing Division, Applied Research Laboratory, is President & CEO, Duncan Parks Enterprises Inc., Lynchburg, TN 37352.

Manuscript submitted March 20, 2001.

Table I. LSA Experimental Parameters

Experiment	Substrate	Matrix Powder	Hard Particle	Laser Scanning Speed ($\times 10^{-3}$ ms^{-1})
Fe-base	4140 steel	Fe	—	6.35
FeWC1	4140 steel	Fe	MC	2.12
FeWC2	4140 steel	Fe	MC	4.23
FeWC3	4140 steel	Fe	MC	6.35
Ni-base	4140 steel	Ni	—	6.35
NiWC1	4140 steel	Ni	MC	2.12
NiWC2	4140 steel	Ni	MC	4.23
NiWC3	4140 steel	Ni	MC	6.35

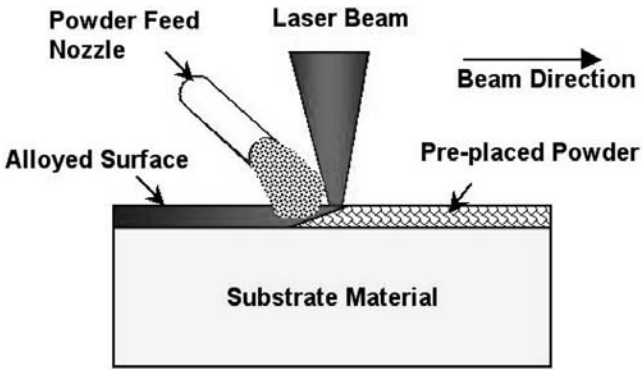

Fig. 1—Schematic illustration of the LSA process.

MC particles to Fe- and Ni-based matrix alloys. In both cases, 4140 steel having a 6.0 mm thickness was utilized as the substrate material. Only spherical powders of iron and nickel, of at least a 99 pct purity and having a size range of 44 to 149 μm (−100 to 325 mesh), were employed as the matrix alloy. However, angular MC powders of 99.7 pct purity, ranging from 44 to 149 μm in size, were used. The iron- and nickel-matrix powders were preplaced on the steel substrate, and the MC powders were gravity fed to the trailing edge of the weld pool (Figure 1).

During LSA, temperatures on the pool surface were measured with a two-wavelength optical pyrometer. In addition, temperatures within the pool were measured with 0.25-mm-diameter W-Re thermocouples which were exposed on the top surface of the substrate through a hole drilled from the bottom surface. The optical pyrometer indicated that surface temperatures on the top surface of the pool exceeded 3273 K; the peak temperature recorded by the thermocouples near the alloy/substrate interface was approximately 1788 K.

III. RESULTS

A. *Laser Surfacing and Microstructure*

Macrographs of LSA bead shapes from the iron-rich system are shown in Figure 2. The beads produced at 6.35 mm s^{-1} with and without MC additions showed no major differences. However, with an increase in laser scanning speed, the bead size became smaller. There was no notable shrinkage or porosity. Detailed observations revealed small cracks in the beads made at slow speeds (2.12 mm s^{-1}). Similar macrographs of the nickel-rich LSA beads are shown in Figure 3. The LSA beads produced at 6.35 mm s^{-1} with an MC addition showed major differences from those produced without the MC addition in nickel-rich LSA beads. The bead without the MC addition showed excessive porosity and shrinkage cracks. Satisfactory LSA beads were obtained at a speed of 2.12 mm s^{-1}. The LSA bead shapes made from the nickel-rich system were wider than those made from the iron-rich system.

Microstructures of LSA beads produced by the iron-rich system at 2.12 mm s^{-1} are shown in Figure 4. The microstructure shows angular MC particles distributed in the matrix. The microstructures around the particles are not homogeneous and contain regions of two-phase dendritic microstructure (gray and white regions) and a single-phase microstructure (white regions). The microstructures from the nickel-rich LSA bead produced at 2.12 mm s^{-1} are shown in Figure 5. The microstructure shows angular MC particles in the matrix and shows preferential dissolution of MC particles. This preferential dissolution leads to a saw-tooth appearance for the MC particles. Detailed microstructural observations indicated some microstructural differences around the particles; however, these differences were limited to a small distance compared with that of iron-rich liquid. Near the carbide interface, white particles can be observed; away from the interface, a two-phase microstructure (gray and white phases) was observed. In addition, black particles resembling graphite in a cast-iron microstructure were observed.

The LSA beads produced at higher laser scanning speeds were analyzed to evaluate the effect of MC particle dissolution in an iron-rich alloy system. In Figure 6, the microstructures of beads produced at 4.23 and 6.35 mm s^{-1} are compared. The microstructures show larger MC particles than those in LSA beads produced at 2.12 mm s^{-1}. Microstructural heterogeneity was present around the MC particles, although to a reduced extent, as the scanning speed increased. The microstructure in an LSA bead produced at 4.23 mm s^{-1} shows a comet-tail shape caused by microstructural heterogeneity along the direction of particle movement. Regions farther away from particles show distinct gray and white two-phase dendritic microstructures. The two-phase microstructure also contained black particles resembling graphite. A detailed examination of the microstructure near the particles showed white particles that may have reprecipitated from the liquid during solidification. A similar microstructure was observed in the LSA beads produced at 6.35 mm s^{-1}. Outlying regions from the particle showed martensitic microstructures instead of two-phase microstructures.

B. *Computational Thermodynamic and Kinetic Calculations*

To understand the microstructural evolution in the LSA process, various phase-stability solidification, and kinetic calculations were performed in iron-tungsten-carbon (Fe-W-C) and nickel-tungsten-carbon (Ni-W-C) alloy systems.

First, ThermoCalc software (version M)[23] was used to perform thermodynamic calculations that determined the phase stability of the various phases in Fe-W-C and Ni-W-C alloy systems at the melting point of a low-alloy steel, *i.e.*, 1800 K. The calculations considered the stability between the following phases: liquid, bcc (ferrite), fcc (austenite), MC (tungsten carbide), graphite, M_6C carbide, and μ phase. The

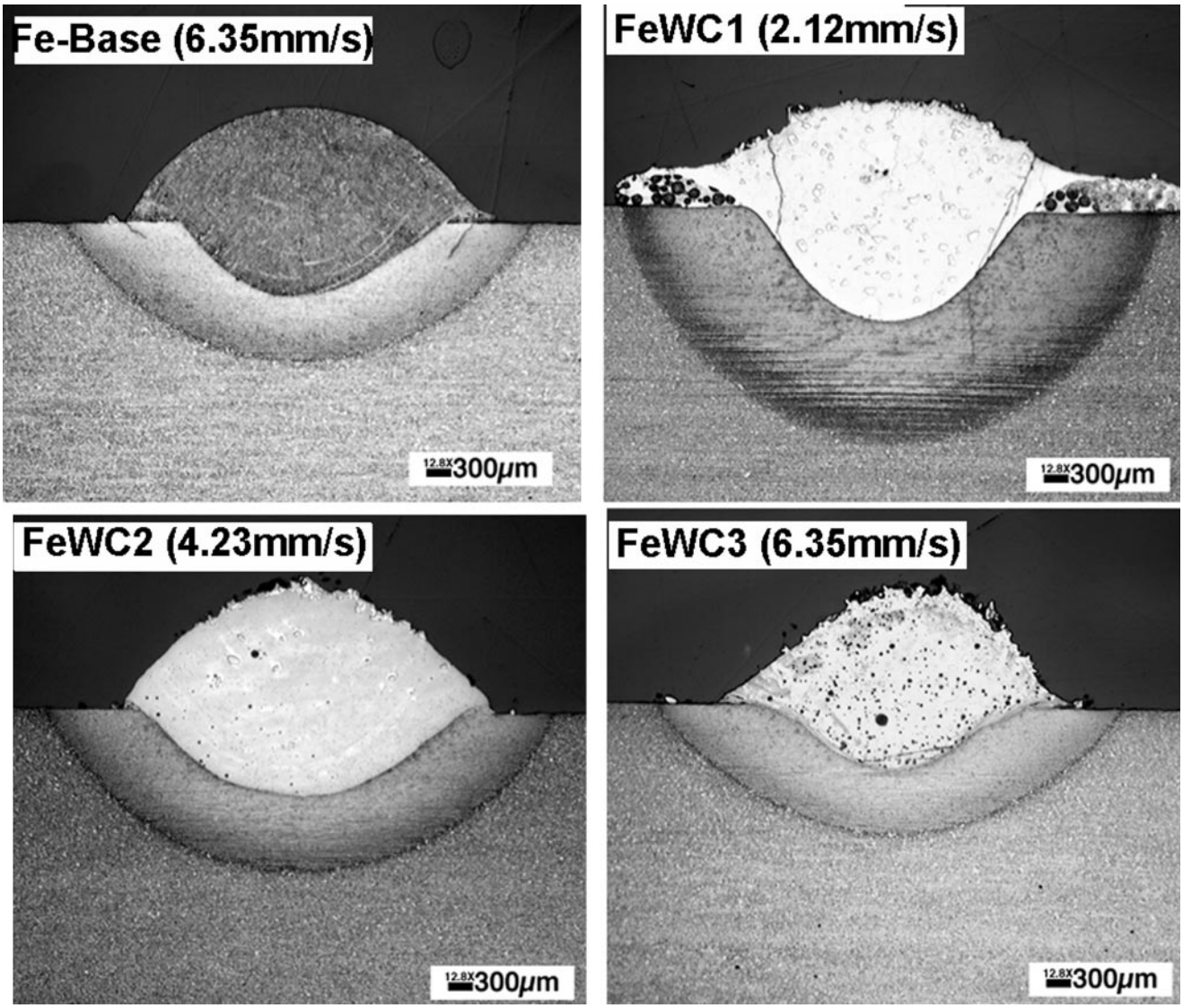

Fig. 2—Macrographs of laser-surface-alloyed bead shapes obtained when preplaced iron powder and tungsten carbide particles were added at the trail ing edge of the laser melt pool at different laser-scanning speeds.

calculated stability regions are shown in Figure 7. The significance of the aforementioned diagram can be understood by considering the typical composition of an Fe-W-C system. If we consider a laser surface containing 20 wt pct MC carbide, the bulk composition would be approximately Fe-10 at. pct W-10 at. pct C. The stability diagram for this Fe-W-C system (Figure 7(a)) showed that only the liquid phase is stable at 1800 K. In contrast, the stability diagram for Ni-10 at. pct W-10 at. pct C showed that both the liquid and MC phases are stable. This result supports the preferential dissolution of MC carbide observed in iron-rich liquid and the higher stability of tungsten carbide in nickel-rich liquid. Even in nickel-rich liquid, the tungsten carbide will dissolve completely if the concentrations of W and C are reduced. Therefore, the stability of these phases is determined by the bulk alloy composition. It is important to note that the bulk composition of the alloy will be affected by the laser scanning speed. A detailed analysis of bulk composition and its relation to laser scanning speed will be presented elsewhere.

The previous thermodynamic calculations can be readily extended for evaluating the reprecipitation of MC carbides during solidification in the LSA deposit. In this case, during LSA, both the matrix and the tungsten carbide melt and constitute a uniform liquid composition at high temperatures ($>$2300 K). Upon cooling, the liquid composition may lead to reprecipitation of tungsten carbide or other phases and/or a different sequence of phase evolution. Scheil assumptions[24] were used to calculate the sequence of phase evolution from the liquid phase. The calculations assumed uniform liquid compositions of Ni-10 at. pct W-10 at. pct C and Fe-10 at. pct W-10 at. pct C at 2300 K. At 2300 K, the liquid phase is the only stable phase for both compositions. The temperature was then lowered in 1 K steps, and the calculations were repeated. After each calculation, the fraction of solid formed was recalculated and the bulk composition was reset to the liquid composition. The calculations were repeated until the thermodynamic equilibrium indicated an absence of liquid. The details of these calculations are given in References 23 and 24; results of the current analysis are shown in Figure 8.

The calculations for the Fe-W-C system showed that the liquid phase remains stable until 1621 K, at which point the

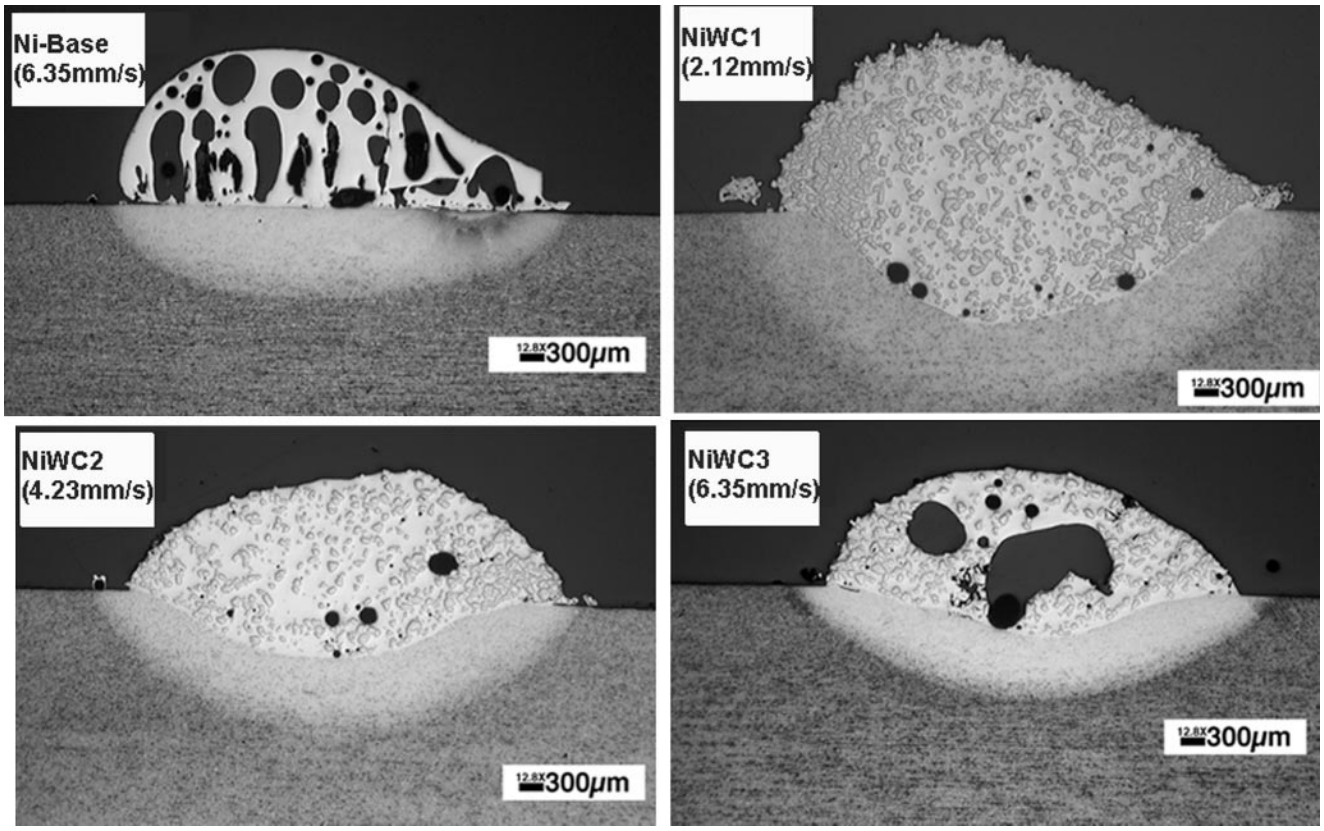

Fig. 3—Macrographs of laser-surface-alloyed bead shapes obtained with preplaced nickel powder and tungsten carbide particles added at the trailin g edge of the laser melt pool at different laser scanning speeds.

calculations indicated that M_6C is the first phase to solidify from liquid. Further cooling leads to the precipitation sequence of fcc (austenite), MC (tungsten carbide), M_6C carbide, and graphite phases due to the change of the liquid composition. The calculated terminal solidification temperature was at 1413 K. In contrast, the calculations for the Ni-W-C system show that the first phase to solidify from the liquid is MC (tungsten carbide) at 1844 K and that further cooling leads to the precipitation of fcc (austenite) and then graphite. The calculated terminal solidification temperature was at 1617 K. Calculations indicate that when the iron-rich liquid solidifies it may contain austenite, M_6C, MC, and graphite, whereas the nickel-rich liquid may contain austenite, MC, and graphite. The nickel-rich liquid does not promote the formation of M_6C carbides. In addition, the nickel-rich alloy system has a higher melting point (1617 K) than that of the iron-rich system (1413 K). Although the thermodynamic calculations are useful in evaluating the reprecipitation of tungsten carbide, they do not yield insight into the dissolution rate of tungsten carbide when it is added to the trailing edge of the liquid pool. Therefore, the diffusion-controlled dissolution rate of the tungsten carbides was estimated as they were introduced into the liquid pool and during subsequent cooling.

The LSA process leads to a wide range of surface temperatures within different regions.[6] Because the tungsten carbide powders can be added to the trailing edges of the molten pools, different carbides may experience different thermal cycles. If the temperature of the tungsten carbide exceeds that of the melting point of tungsten carbide, there will be competition between the dissolution and melting phenomena.[25] In those cases, melting will be governed by the heat-transfer conditions. Since the powders are added in the trailing edge of the weld pool, where the temperature may be lower than 2300 K, the primary melting of tungsten carbide is not expected. In addition, if the particles are transported by fluid flow, they may experience a complex thermal cycle. Therefore, to describe the dissolution of MC particles, the following parameters are necessary: peak temperature, temperature-time history, and the local composition of the liquid. Experimental descriptions of these parameters for all particles are difficult and often impossible. However, computational heat-transfer fluid-flow models have been used to describe these parameters[22] in liquid welds when the growth and dissolution of Al_2O_3 inclusions in weld pools are being considered. The apparent movements of particles are, indeed, observed in our experiments (Figure 6(a)). The extension of these models to the present experiment is extremely difficult, because of the complexities involved in tungsten carbide impingement on the laser-melt surface and local compositional gradients caused by dissolution. Therefore, in this work, the following assumptions were made to describe the dissolution of a single tungsten carbide particle.

The tungsten carbide was assumed to enter the liquid pool at a temperature of 2300 K. This starting temperature is an assumption, and, as mentioned earlier, the particles may experience higher temperatures at laser-impingement areas. However, based on the previous work, the maximum temperature of the powder that is added at the trailing edge of the weld pool is expected to be 2300 K or lower. Then, the

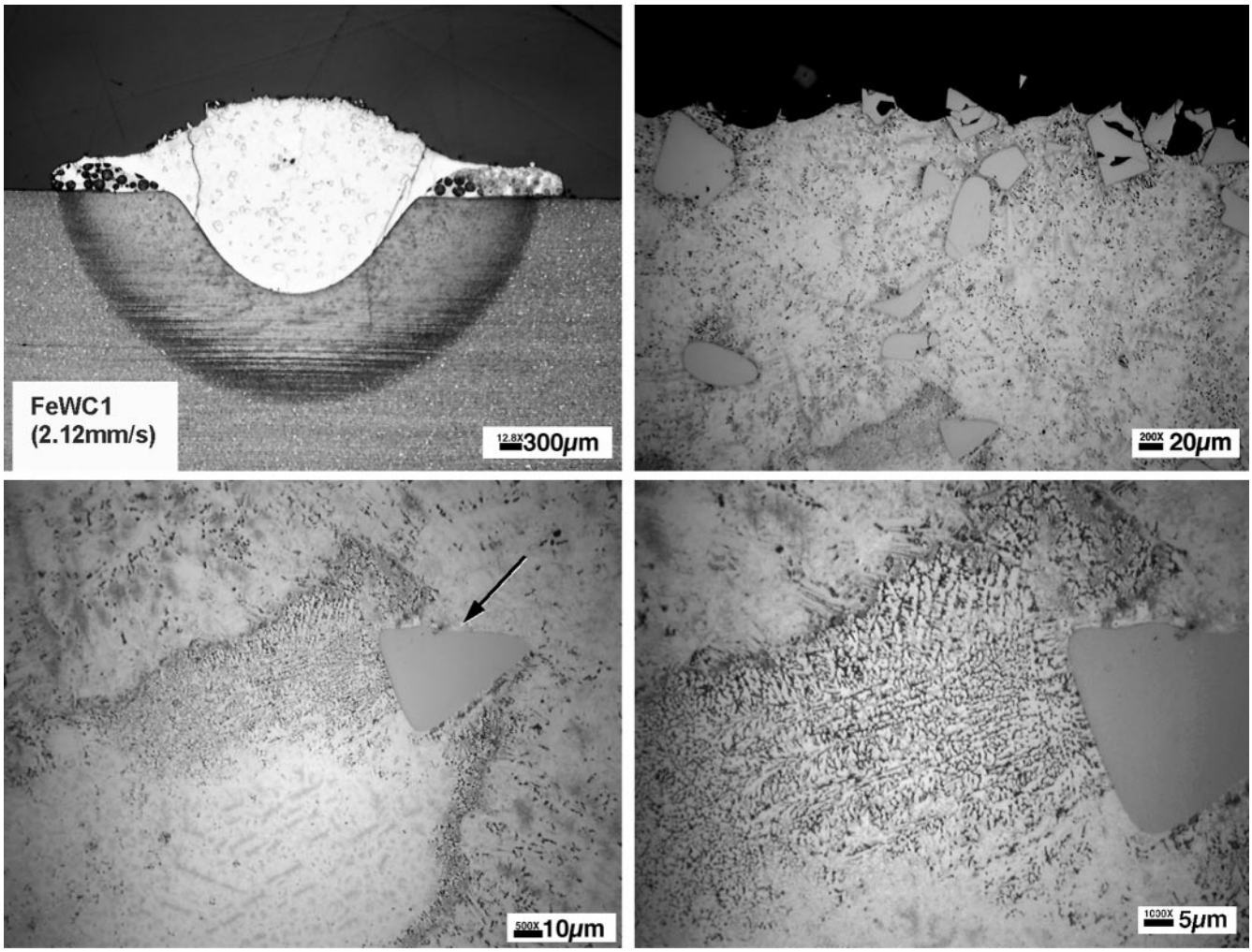

Fig. 4—Detailed microstructural observations from laser-surface-alloyed sample FeWC1. The arrow shows a typical tungsten carbide particle.

particle and the surrounding liquid were assumed to cool at 100 K s^{-1} to a temperature of 1800 K. This cooling rate is based on preliminary measurements made by thermocouple measurements in other experiments. The initial composition of the liquid was assumed to be pure iron or pure nickel. The calculations assumed a local equilibrium at the interface. One-dimensional diffusion-controlled growth or dissolution was performed to evaluate the stability of MC (tungsten carbide) as the liquid cools to a lower temperature. The schematic illustration of the geometry used for diffusion-controlled growth calculations is shown in Figure 9. The initial size of the MC carbide was 100 μm, and the interparticle spacing was 1000 μm. The calculation methodology allows for complete dissolution, redistribution of alloying elements within the liquid region, and the reprecipitation of MC carbide at the right-hand side of the geometry, as shown in Figure 9. In these calculations, the barrier for nucleation (surface energy and critical radius) is not considered. Therefore, the reprecipitation of MC carbide from liquid is, essentially, decided when thermodynamic conditions are satisfied. The calculations ignore the effect of dendrite-tip undercooling, because estimating it is uncertain for these LSA process conditions. The model does not consider the formation of nonstoichiometric carbides and, therefore, ignores diffusion within the carbide.

DicTra software[26,27] and a standard solid-solution database and mobility database[23,27] were used to perform the calculations. The nominal diffusivity of alloying elements in liquid steel is assumed to be constant ($D_M = 1 \times 10^{-9}$ $m^2\ s^{-1}$) for all the elements. The calculations also considered the effect of enhanced diffusion of alloying elements due to fluid flow by increasing the diffusivity arbitrarily to a value of $D_M = 1 \times 10^{-6}\ m^2\ s^{-1}$. The results of kinetic calculations are presented in Figures 10 through 13. The calculated positions of the MC/liquid interface with nominal diffusivity are shown in Figure 10. The results indicate that the interface moves to the right from its initial position, indicating dissolution (Figure 9); however, complete dissolution was not predicted. The dissolution rate of MC carbide in a nickel-rich liquid was lower than the rate in an iron-rich liquid. The concentration profiles of W and C in the liquid ahead of the interface are shown in Figure 11. The results from the Fe-W-C and Ni-W-C systems indicate that the concentrations of W and C vary from a local equilibrium value to that of bulk concentrations over a distance of 100 to 200 μm. There were no significant differences in the shape of these concentration profiles, except for the magnitudes. In general, the concentrations of W and C near the interface were higher in the iron-rich liquid than in the nickel-rich liquid.

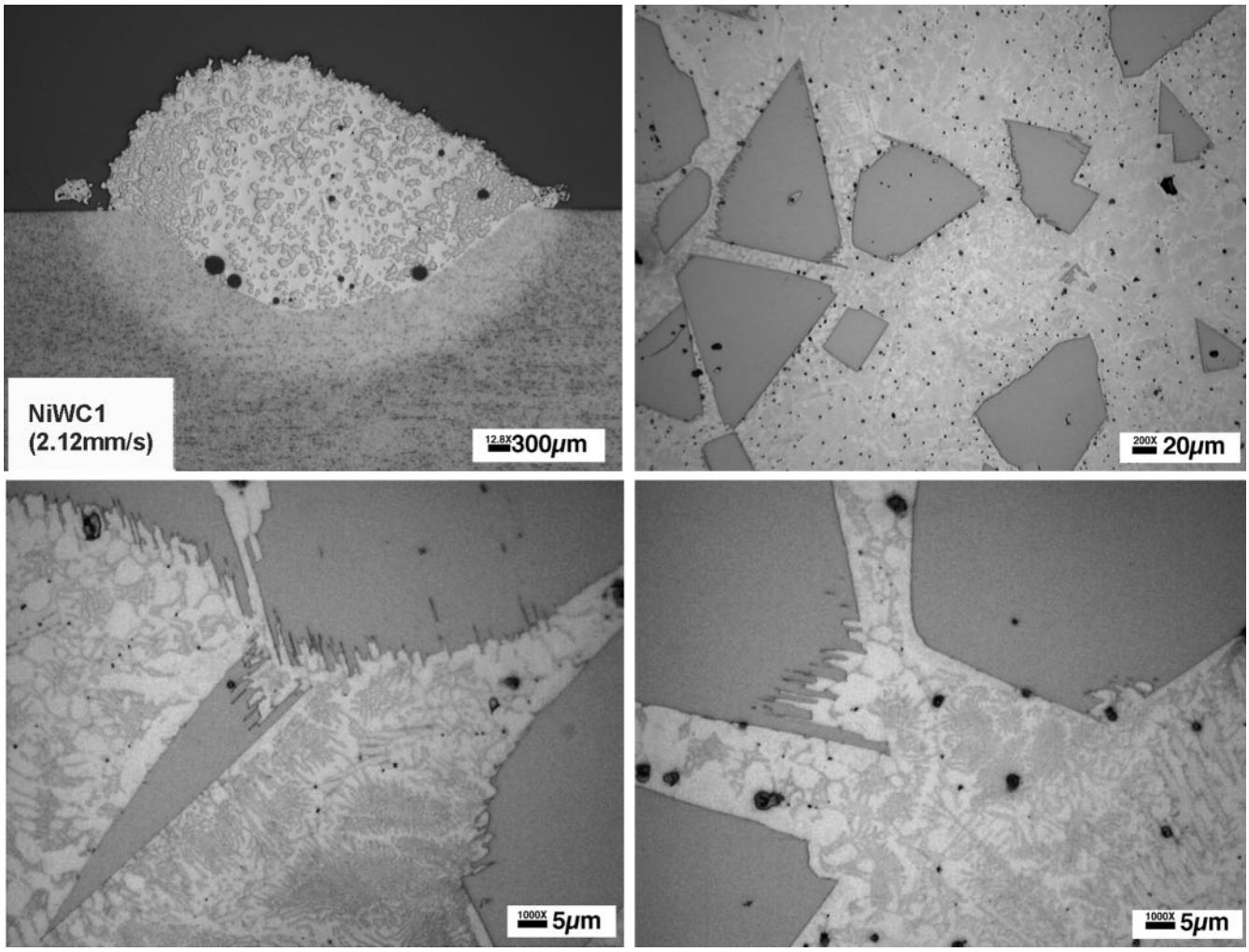

Fig. 5—Detailed microstructural observations from laser-surface-alloyed sample NiWC1. The tungsten carbides indicate faceted morphology.

The calculated positions of the MC/liquid interface with enhanced diffusivity are shown in Figure 12. In the Fe-W-C system, the MC dissolved at a rapid rate, and dissolution was complete at 2295 K. Further cooling did not lead to any reprecipitation of MC. In contrast, in the Ni-W-C system, MC dissolved rapidly; however, complete dissolution was indicated at 2271 K. In addition, the calculations based on further cooling indicated that the reprecipitation of MC carbides occurred at 2197 K. Further cooling led to MC carbide growth to 41 μm at 1800 K. The results show that the MC carbides in the Ni-W-C system have a low dissolution rate even with enhanced diffusivity, and that they have enhanced stability at high temperatures. The concentration profiles in both the Fe-W-C and Ni-W-C systems with enhanced diffusivity are shown in Figure 13 and are flatter then those observed in Figure 11. This is due to the overlap of diffusion profiles at the origin (0 μm of diffusion geometry), as indicated by the increase in the W and C concentration.

IV. DISCUSSION

The macrostructural observations show that the LSA bead morphology in an iron-rich system is different from that in a nickel-rich system (compare Figures 2 and 3). The nickel-rich liquid does not wet the 4140 steel substrate as effectively as does the iron-rich liquid. Reasons for the inefficient wetting by nickel-rich liquid are unknown, but are thought to be the effect of variations in surface tension with temperature. Due to differences in bead morphology, the heat-affected zone in the substrate also appears to be less pronounced. Further theoretical work involving computational heat-transfer and fluid-flow models is needed to understand the differences in LSA-zone shape changes.

Microstructures from iron-rich liquid indicate dissolution of tungsten carbide particles in LSA beads and an associated microstructural heterogeneity (Figure 4). The microstructural heterogeneity appears to be enhanced in certain directions when the laser traversing speed increased (Figure 6(a)), which seems to indicate that the concentration gradients may have been present before solidification was complete. The apparent enhancement is supported by the comparison of microstructural heterogeneity in LSA beads produced at 4.23 and 6.35 mm s^{-1}. In both the cases, the microstructures near the interface show white particles, which may have formed during solidification. However, the microstructure farther away from the interface in LSA beads produced at 4.23 mm

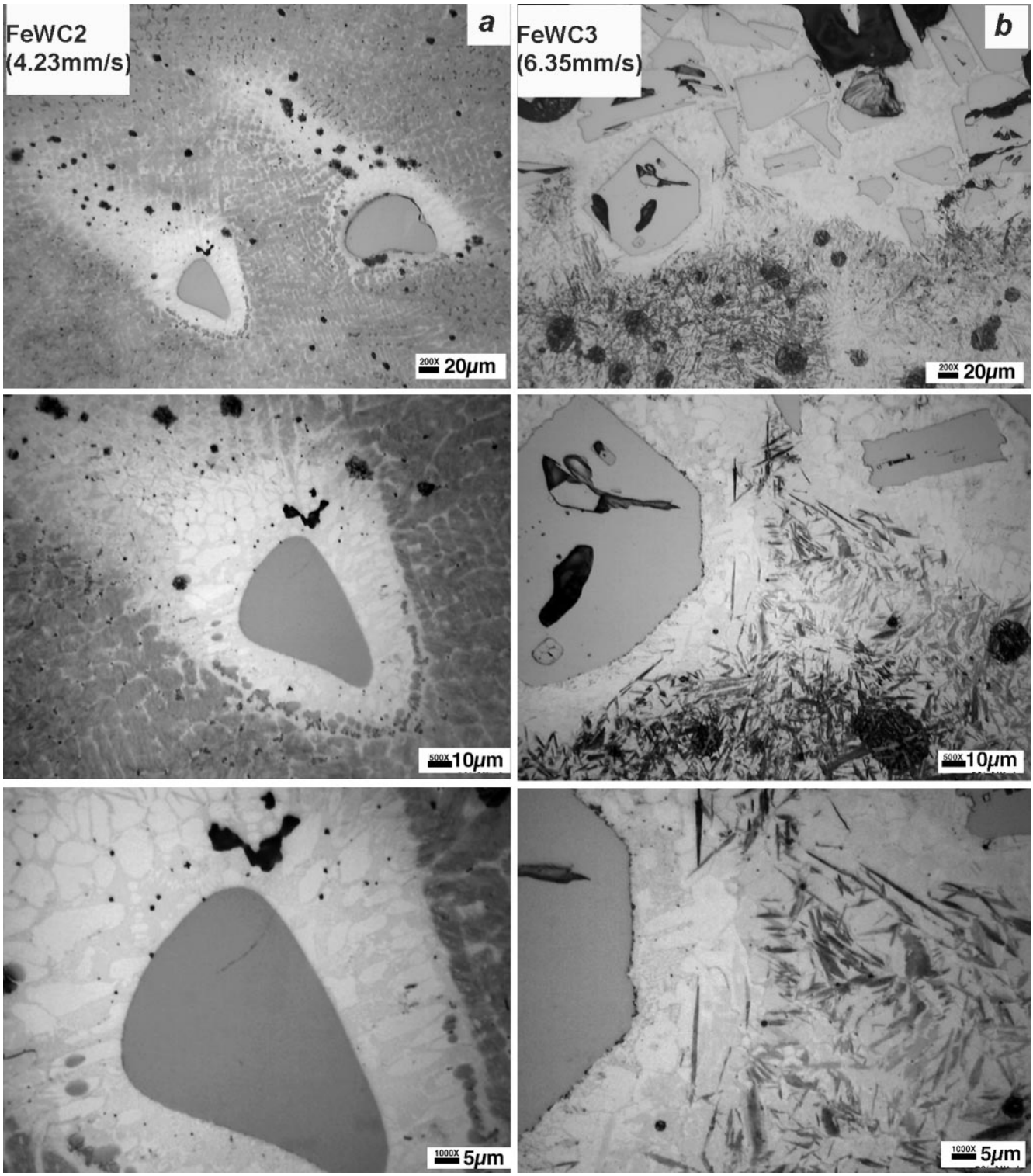

Fig. 6—Microstructure from laser-surface-alloyed samples (*a*) FeWC2-4.23 mm s^{-1} and (*b*) FeWC3-6.35 mm s^{-1}.

s^{-1} contains a two-phase dendritic microstructure, whereas the microstructure in the case of LSA beads produced at 6.35 mm s^{-1} contains martensite. This difference can be explained by the following discussion. At slower laser traversing speeds, the dissolution of a tungsten carbide particle will lead to enrichment of the interparticle regions with carbon because the time available for diffusion increases. This enrichment is due to an overlap of diffusion profiles from adjacent particles. The enriched carbon and tungsten will promote the eutectic formation of austenite and carbide from liquid, thus forming a two-phase microstructure. However, at faster laser scanning speeds, the time available for redistribution would be reduced, thus causing less enrichment of carbon in the interparticle regions. In such cases,

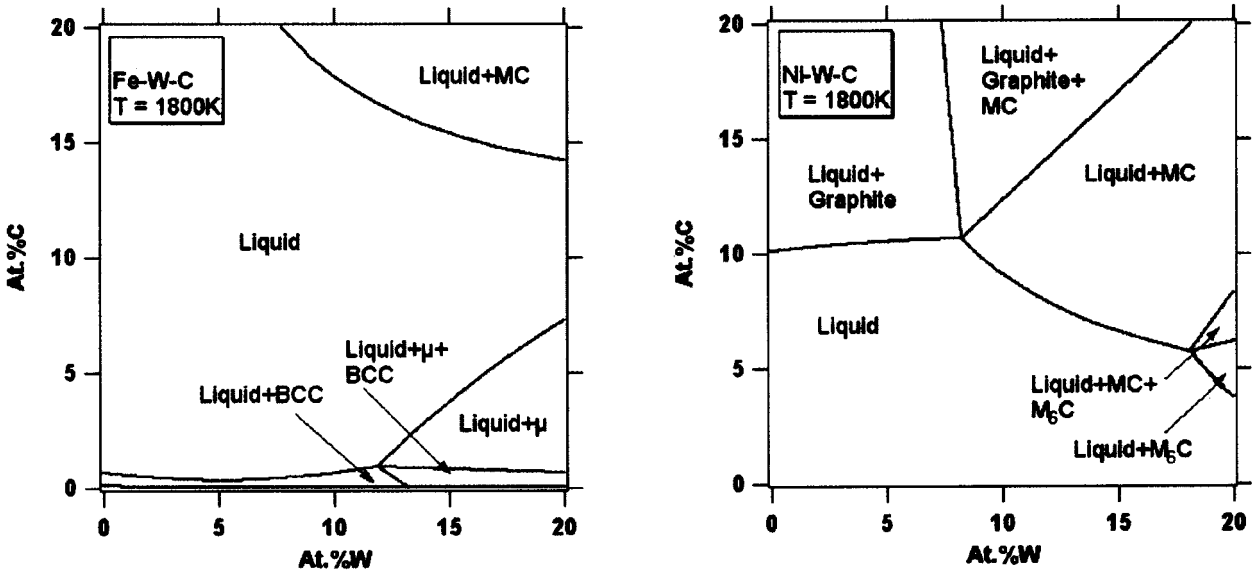

(*a*) (*b*)

Fig. 7—Comparison of calculated phase boundary regions for ternary alloy system at 1800 K: (*a*) Fe-W-C system and (*b*) Ni-W-C system.

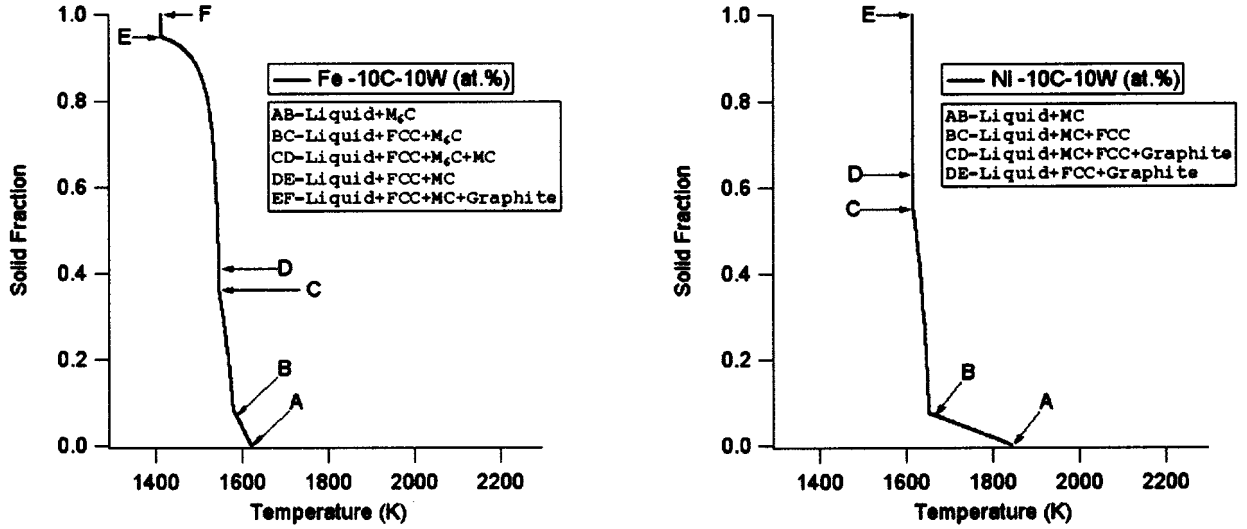

(*a*) (*b*)

Fig. 8—Comparison of phase evolution during solidification in two ternary alloy systems calculated using Scheil assumption: (*a*) Fe-10 at. pct W-10 at. pct C system and (*b*) Ni-10 at. pct W-10 at. pct C system.

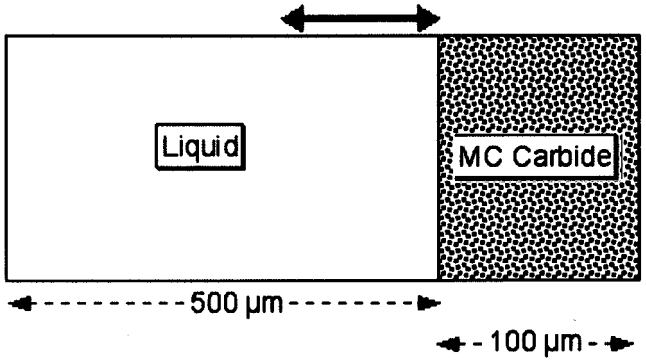

Fig. 9—Schematic illustration of the one-dimensional diffusion geometry used to calculate the diffusion-controlled dissolution of tungsten carbide (MC) in a liquid pool as it cools from 2300 to 1800 K at a rate of 100 K s^{-1}.

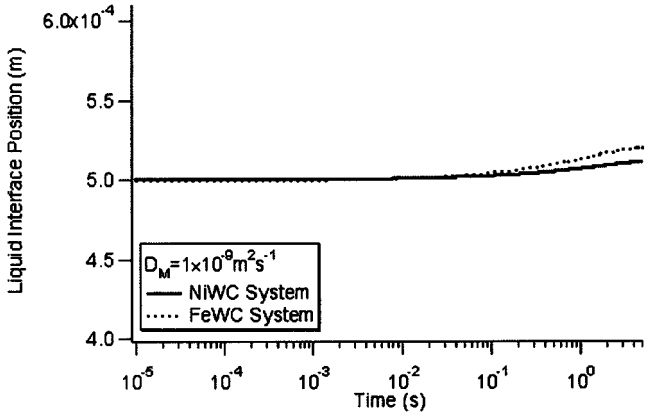

Fig. 10—Predicted position of the interface between liquid and MC carbi de as a function of time with assumed diffusivity of 1×10^{-9} m^2 s^{-1}.

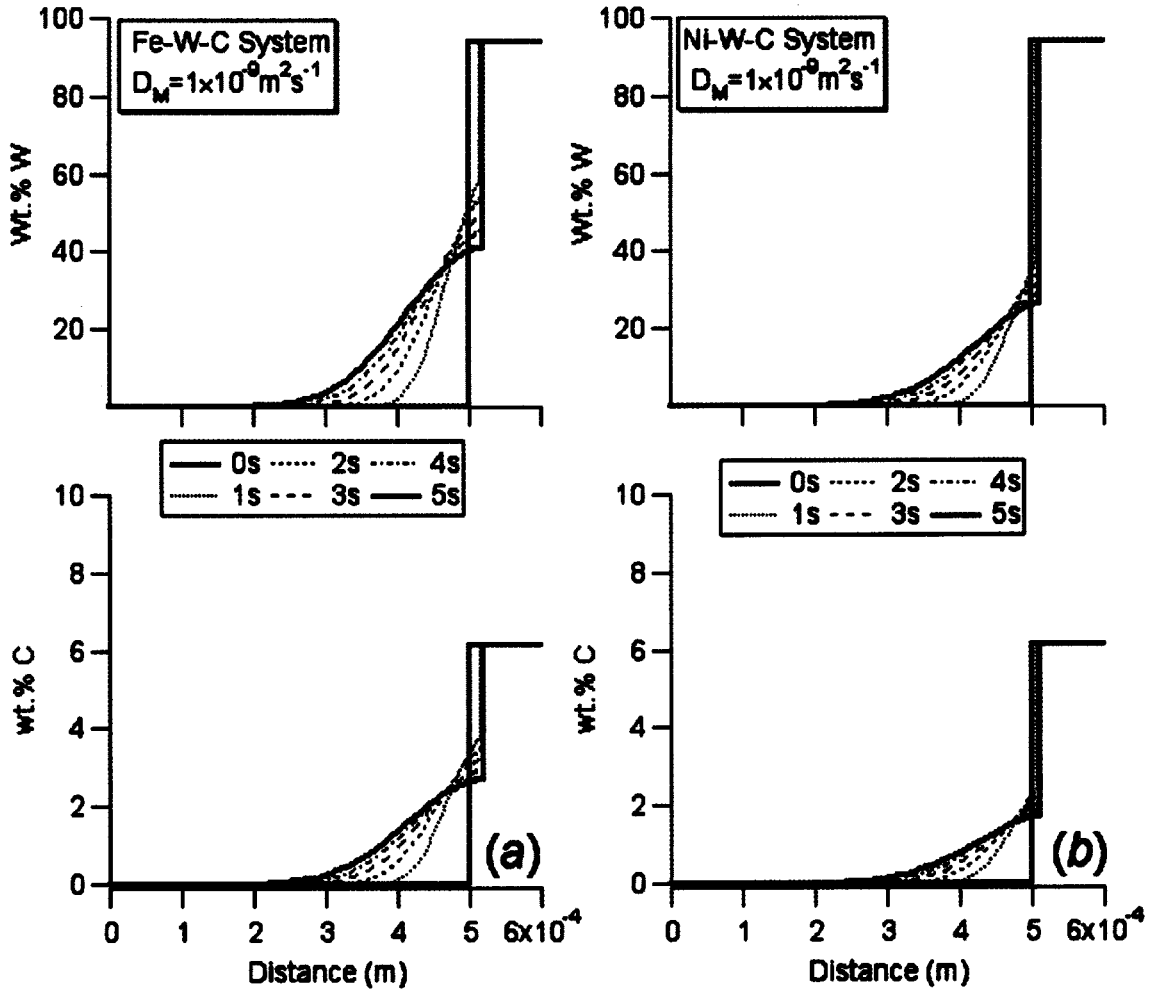

Fig. 11—Calculated tungsten and carbon concentration profiles in the liquid melt pool (left side) in contact with MC carbide (right side) as a function of time. The diffusivity of atoms in liquid is assumed to be 1×10^{-9} m^2 s^{-1}: (*a*) Fe-W-C and (*b*) Ni-W-C.

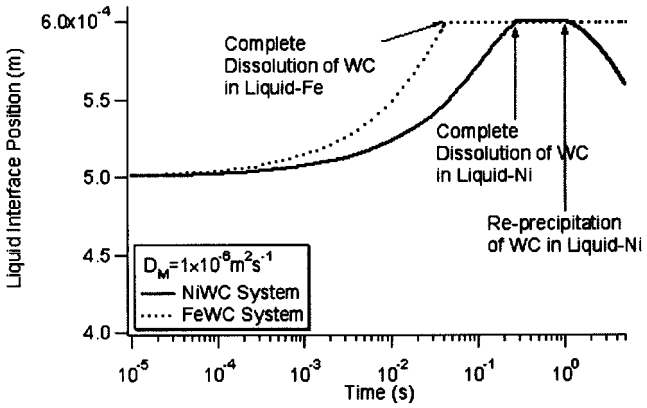

Fig. 12—Predicted position of interface between liquid and MC carbide as a function of time with assumed diffusivity of 1×10^{-6} m^2 s^{-1}.

the outlying matrix (away from the particle) may not induce a eutectic reaction, but rather may undergo the traditional solidification of liquid to austenite and the subsequent solid-state decomposition to martensite.

A qualitative comparison of the microstructure for a given laser traversing speed indicates a higher retention of tungsten carbide particles in the nickel-rich system than in the iron-rich system (Figures 4 and 5). The dissolution of MC particles in the nickel-rich system leads to microstructural heterogeneity in the surrounding matrix, similar to that in an iron-rich liquid. White particles were observed near the interface, and a two-phase (gray and white) dendritic microstructure was observed away from the particles. This microstructural evolution is supported by the diffusion-controlled kinetic calculations (Figure 10). The angular shapes of the particles are maintained even after laser processing. The exact mechanisms for the formation of a saw-tooth appearance of the carbide interface remain to be explained. These interfaces may result from the regrowth of the originally regressing interface due to dissolution (Figure 12) or interface instability during solidification conditions.[31]

The concentration profiles calculated for the high- and low-diffusivity assumptions qualitatively support the microstructural heterogeneity around the MC particle (Figure 11). The concentration gradients around the MC particles are strongly affected by the diffusivity of atoms in the liquid. For example, the diffusivity may be enhanced due to fluid flow. The present work demonstrates that this enhanced diffusivity would lead to mixing of liquid, thereby reducing the concentration gradients around the particles (Figure 13).

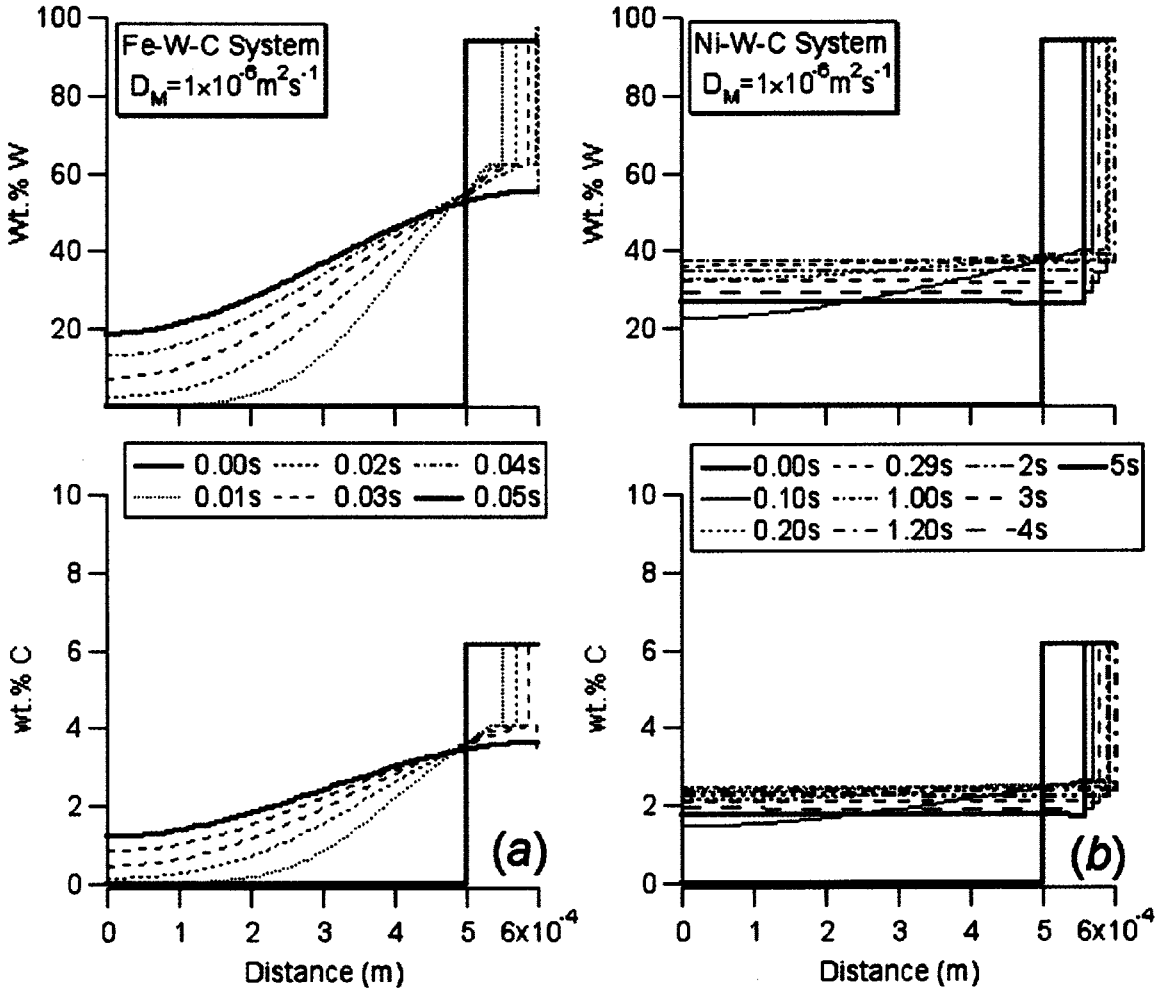

Fig. 13—Calculated tungsten and carbon concentration profiles in the liquid melt pool (left side) in contact with MC carbide (right side) as a function of time. The diffusivity of atoms in liquid is assumed to be 1×10^{-6} m^2 s^{-1}: (*a*) Fe-W-C and (*b*) Ni-W-C.

These concentration gradients, if not removed, may lead to large changes in microstructure, as suggested by Scheil solidification calculations (Figure 8). The sensitivity of the phase evolution during solidification was further evaluated with thermodynamic calculations of different Fe-W-C and Ni-W-C compositions. Liquid compositions predicted near the interparticle regions (Fe-18.7W-1.22C (wt pct) and Ni-36.3W-2.37C (wt pct)) were considered in this analysis. The solidification calculations using the method given before are shown in Figure 14. The results are consistent with the results from Figure 8, in that the melting points of the iron-rich alloy system are lower than those of the nickel-rich alloy system. However, the phase evolution in both alloys changed. In the case of iron-rich liquid, the first phase to solidify is fcc (austenite) rather than M_6C carbide. In case of the nickel-rich liquid, the first phase to solidify is, surprisingly, graphite, followed by the precipitation of the MC carbides. The microstructures from the nickel-rich liquid indicated some black particles which may be graphite (Figure 5); however, further characterization by X-ray diffraction and scanning electron microscopy is needed to confirm this theory. The relationship between the local composition and phase evolution is important for maintaining the cracking resistance of the LSA regions during reheating that may occur during subsequent bead processing. The results of these calculations suggest a method by which a uniform microstructure around the MC particles can be promoted by controlling the fluid flow to enhance the diffusion.

The results of this study indicate that the computational thermodynamic and kinetic tools can be applied as a design tool for the LSA processes that were tested. However, the application of these models for generalized microstructural predictions needs further work for the following reasons. The microstructures produced in these processes need to be characterized with X-ray diffraction, transmission electron microscopy, and compositional mapping with energy-dispersive spectroscopy to evaluate the predicted values, which is part of an on-going research effort. In addition, the microstructure content of the alloys produced by the rapid cooling conditions of the LSA process is different than the microstructural content that is produced under slow weld cooling conditions.[28] The computational thermodynamic calculations discussed in this article cannot be readily applied to conditions involving nonequilibrium conditions or nonequilibrium solubility.[29,30] In addition, computational thermodynamic models need to be extended to describe the amorphous phase formation and must be coupled with the dendrite growth theories for laser-processing conditions.[31] One should be able to predict interface stabilities by coupling

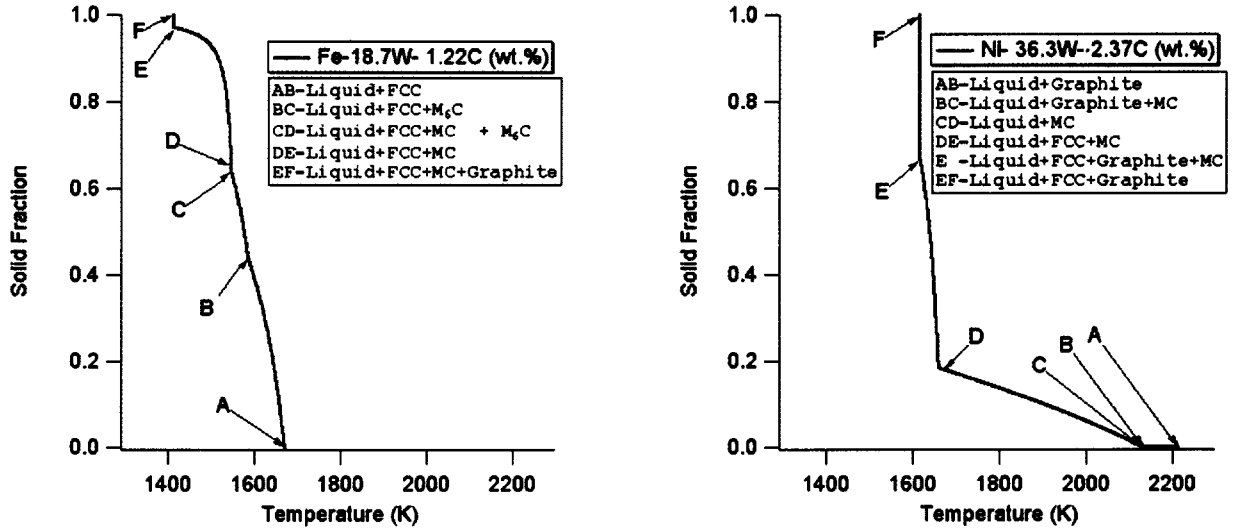

(*a*) (*b*)

Fig. 14—Comparison of phase evolution during solidification in two ternary alloy systems calculated using the Scheil assumption: (*a*) Fe-18.7 wt pct W-1.22 wt pct C system and (*b*) Ni-36.3 wt pct W-2.37 wt pct C system.

solidification theories with multiple-component thermodynamics. Doing so would enable an understanding of the different dendrite morphologies observed in this research.

V. CONCLUSIONS

The microstructural evolution during LSA with tungsten carbide particles in iron-rich and nickel-rich alloy systems was investigated on a low-alloy steel substrate. The LSA bead morphologies in the two systems were observed to be significantly different from each other.

Observations of the microstructure in these systems indicated that dissolution of tungsten carbide particles in iron-rich liquids was faster than that in nickel-rich liquids for identical laser traversing speeds. The dissolution of tungsten carbide particles in iron-rich liquid became less pronounced with an increase in the laser traversing speed. Microstructural heterogeneity was observed around the tungsten carbide particles in both alloy systems. In the case of nickel-rich liquid, tungsten carbide particles developed complex, faceted surfaces.

The enhanced stability of the tungsten carbide phase in nickel-rich liquid was related to thermodynamic stability. Thermodynamic calculations indicated that tungsten carbide precipitates from the liquid upon cooling, although tungsten carbide particles dissolve in nickel-rich liquid. However, in the case of iron-rich liquid, if the tungsten carbide particles dissolve, other carbides such as M_6C may form instead of the MC particles during cooling.

Diffusion-controlled dissolution of tungsten carbide in both iron-rich and nickel-rich liquid was calculated for a cooling rate of 100 K s^{-1} while cooling from 2300 to 1800 K. At nominal diffusivity levels (1×10^{-9} m^2 s^{-1}), the calculations indicate a partial dissolution of tungsten carbide and concentration gradients ahead of the carbide interface in the liquid region. Further calculations with higher diffusivity levels (1×10^{-6} m^2 s^{-1}) led to complete dissolution of MC particles in both iron- and nickel-rich liquids, with negligible concentration gradients in the liquid. The regrowth of tungsten carbide particles was calculated before the liquid reached 1800 K, in the case of the nickel-rich liquid.

ACKNOWLEDGMENTS

This research was sponsored by the Division of Materials Sciences and Engineering and Assistant Secretary for Energy Efficiency and Renewable Energy (MPLUS Program), Office of Industrial Technologies, Advanced Industrial Materials Program, United States Department of Energy, under Contract No. DE-AC05-00OR22725 with UT-Battelle, LLC. The laser processing experiments were sponsored by the Laser Processing Consortium and were conducted at the Applied Research Laboratory, Pennsylvania State University. The authors thank Drs. C.A. Blue and Q. Han for helpful discussions.

REFERENCES

1. A. Glozman and M. Bamberger: *Metall. Mater. Trans. A*, 1997, vol. 28A, 1699-1703.
2. J.M. Pelletier, F. Oucherif, P. Sallamand, and A.B. Vannes: *Mater. Sci. Eng.*, 1995, vol. A202, pp. 142-47.
3. G. Ricciardi, M. Cantello, G. Molino, W. Varani, and E. Carlet: *Key Eng. Mater.*, 1990, vol. 46, p. 415.
4. G. Dehm, C. Scheu, and M. Bamberger: *Proc. Conf. on Laser Materials Processing, LIA*, 1997, vol. 2, p. F-128.
5. I. Goldfarb and Bamberger: *Scripta Mater.*, 1996, vol. 34, pp. 1051-57.
6. R. Ebner, W. Pitscheneder, R. Benes, T. DebRoy, and K. Mundra: *Proc. 2nd Int. Austria-Israel Technion Symp. and Industrial Forum*, Graz, June 4–6, 1997, Austrian Technion Society, Vienna, 1997, pp. 79-93.
7. C. Zhenda, L.L. Chew, and Q. Ming: *J. Mater. Processing Technol.*, 1996, vol. 62, pp. 321-23.
8. J.D. Mazumdar, A. Weisheit, B.L. Mordike, and I. Manna: *Mater. Sci. Eng. A*, 1999, vol. A266, pp. 123-34.
9. J.D. Mazumdar and I. Manna: *Mater. Sci. Eng. A*, 1999, vol. A268, pp. 227-35.
10. J.D. Mazumdar and I. Manna: *Mater. Sci. Eng. A*, 1999, vol. A267, pp. 50-59.
11. E. Gemelli, A. Galerie, and M. Caillet: *Solid State Ionics*, 1997, vol. 95, pp. 81-86.

12. M. Riabkina-Fishman and J. Zahavi: *Appl. Surf. Sci.*, 1996, vol. 106, pp. 263-67.
13. C. Tassin, F. Laroudie, M. Pons, and L. Lelait: *Surf. Coatings Technol.*, 1996, vol. 80, pp. 207-10.
14. I. Manna, W.M. Steen, and K.G. Watkins: *Scripta Mater.*, 1997, vol. 37, 561-68.
15. M. Riahi: *J. Mater. Processing Technol.*, 1996, vol. 58, pp. 3-12.
16. S.M. Zhu, L. Wang, G.B. Li, and S.C. Tjong: *Mater. Sci. Eng. A*, 1995, vol. A201, pp. L5-L7.
17. R. Colaco, C. Pino, and R. Vilar: *Scripta Mater.*, 1999, vol. 41, pp. 715-21.
18. R.P. Martukanitz: Applied Research Laboratory, The Pennsylvania State University, PA, unpublished research, 2000.
19. K. Mundra, T. DebRoy, S.S. Babu, and S.A. David: *Welding J.*, 1997, vol. 76, pp. 163s-171s.
20. S.S. Babu, S.A. David, J.M. Vitek, K. Mundra, and T. DebRoy: *Mater. Sci. Technol.*, 1995, vol. 11, pp. 186-99.
21. S.S. Babu, S.A. David, J.M. Vitek, K. Mundra, and T. DebRoy: *Sci. Technol. Welding Joining*, 1999, vol. 4, pp. 276-84.
22. T. Hong, T. DebRoy, S.S. Babu, and S.A. David: *Metall. Trans. B*, 2000, vol. 31B, pp. 161-69.
23. B. Sundman, B. Jansson, and J.O. Andersson: *CALPHAD*, 1985, vol. 9, pp. 1-153.
24. K.C. Hsieh, S.S. Babu, J.M. Vitek, and S.A. David: *Mater. Sci. Eng.*, 1996, vol. A215, pp. 84-91.
25. Q. Han and A. Hellawell: *Metall. Mater. Trans. B*, 1997, vol. 28B, pp. 169-73.
26. J.-O. Andersson, L. Höglund, B. Jönsson, and J. Ågren: in *Fundamentals and Applications of Ternary Diffusion*, G.R. Purdy, ed., Pergamon Press, New York, NY, 1990, pp. 153-63.
27. A. Engström, L. Höglund, and J. Ågren: *Metall. Mater. Trans. A*, 1994, vol. 25A, pp. 1127-34.
28. M.A. Anjos, R. Vilar, R. Li, M.G. Ferreira, W.M. Steen, and K. Watkins: *Surf. Coatings Technol.*, 1995, vol. 70, pp. 235-42.
29. S.C. Tjong, J.S. Ku, and N.J. Ho: *Surface Coating Technol.*, 1997, vol. 90, pp. 203-09.
30. Y. Isshiki, K. Mizumoto, and M. Hashimoto: *Thin Solid Films*, 1998, vol. 317, pp. 468-80.
31. W. Guo and A. Kar: *Acta Mater.*, 1998, vol. 46, pp. 3485-90.